Journal of Physics D: Applied Physics

Sonication-assisted liquid exfoliation and size-dependent properties of magnetic two-dimensional α-$RuCl_3$

OPEN ACCESS
IOP Publishing
Journal of Physics D: Applied Physics
J. Phys. D: Appl. Phys. **56** (2023) 274001 (12pp)
https://doi.org/10.1088/1361-6463/accc3e

Sonication-assisted liquid exfoliation and size-dependent properties of magnetic two-dimensional α-$RuCl_3$

Kevin Synnatschke[1,2,*], Martin Jonak[3], Alexander Storm[4], Sourav Laha[5,6], Janis Köster[4], Julian Petry[1], Steffen Ott[1], Beata Szydłowska[7], Georg S Duesberg[7], Ute Kaiser[4], Rüdiger Klingeler[3], Bettina V Lotsch[5] and Claudia Backes[1,8,*]

[1] Applied Physical Chemistry, Heidelberg University, Im Neuenheimer Feld 253, 69120 Heidelberg, Germany
[2] School of Physics, University of Dublin, Trinity College, Dublin 2, Ireland
[3] Kirchhoff Institute for Physics, Heidelberg University, Im Neuenheimer Feld 227, 69120 Heidelberg, Germany
[4] Central Facility of Electron Microscopy, Electron Microscopy Group of Materials Science, Ulm University, Albert-Einstein-Allee 11, 89081 Ulm, Germany
[5] Department of Nanochemistry, Max Planck Institute for Solid State Research, Heiseberg-Str. 1, Stuttgart 70569, Germany
[6] Department of Chemistry, National Institute of Technology Durgapur, Mahatma Gandhi Avenue, Durgapur 713209, West Bengal, India
[7] Insitute of Physics, EIT 2, Faculty of Electrical Engineering and Information Technology, University of the Bundeswehr Munich & SENS Research Center, Werner-Heisenberg-Weg 39, Neubiberg 85577, Germany
[8] Physical Chemistry of Nanomaterials, Kassel University, Heinrich-Plett Str. 40, 34132 Kassel, Germany

E-mail: synnatsk@tcd.ie and backes@uni-kassel.de

Received 28 November 2022, revised 20 March 2023
Accepted for publication 12 April 2023
Published 26 April 2023

Abstract

Originating from the hexagonal arrangement of magnetic ions in the presence of strong spin orbit coupling, α-$RuCl_3$ is considered as model system for the Kitaev-Heisenberg model. While the magnetic properties of α-$RuCl_3$ have been studied in bulk single crystals or micromechanically-exfoliated nanosheets, little is known about the nanosheets' properties after exfoliation by techniques suitable for mass production such as liquid phase exfoliation (LPE). Here, we demonstrate sonication-assisted LPE on α-$RuCl_3$ single crystals in an inert atmosphere. Coupled with centrifugation-based size selection techniques, the accessible size- and thickness range is quantified by statistical atomic force microscopy. Individual nanosheets obtained after centrifugation-based size selection are subjected to transmission electron microscopy to confirm their structural integrity after the exfoliation. The results are combined with bulk characterisation methods, including Raman and x-ray photoelectron spectroscopy, and powder diffraction experiments to evaluate the structural integrity of the nanosheets. We report changes of the magnetic properties of the nanomaterial with nanosheet size, as well as photospectroscopic metrics for the material concentration and average layer number.

* Authors to whom any correspondence should be addressed.

Finally, a quantitative analysis on environmental effects on the nanomaterial integrity is performed based on time and temperature dependent absorbance spectroscopy revealing a relatively slow decay (half-life of ∼2000 h at 20 °C), albeit with low activation energies of 6–20 kJ mol^{-1}.

Supplementary material for this article is available online

Keywords: liquid phase exfoliation, $RuCl_3$, 2D material, size selection, nanomaterial stability

(Some figures may appear in colour only in the online journal)

1. Introduction

Layered ruthenium chloride (α-$RuCl_3$) is a candidate for the Kitaev-Heisenberg model due to a triangular arrangement of magnetic ions and strong relativistic spin–orbit coupling. The spin-1/2 model with bond-dependent spin interactions features a quantum spin liquid (QSL) ground state, which can be considered as topological state with the potential for coherent transport of quantum information and fractional excitations [1–4]. The latter can be understood as exotic phenomenon which splits an electron into well-defined quasiparticles. In case of a Kitaev 2D-honeycomb lattice, this supports the formation of gauge fluxes and Majorana fermions [5]. While fractional excitation is only reported in theory as yet, the prospect of experimental realisation of such interactions in α-$RuCl_3$ (or any material) could be considered as breakthrough in quantum computation technology [6].

However, apart from such exotic interactions, non-Kitaev interactions in $RuCl_3$ yield long-range antiferromagnetic order at low temperatures [1]. The ordering in single crystals has previously been found to proceed via a single sharp phase transition at a Neel temperature of $T_N = 7$ K as seen in magnetic susceptibility and specific heat measurements [1] or via a sequence of two phase transitions occurring at $T_{N1} \approx 14$ K, and $T_{N2} \approx 8$ K, respectively [7–10]. It has been argued that the number, position, and shape of the magnetic transitions changes as a function of stacking order and stacking faults of the hexagonal layers of Ru^{3+} ions in single-crystalline samples. In polycrystalline samples however, single antiferromagnetic phase transitions are reported at $T_N = 11$ K [11], $T_N = 13$ K [12], and $T_N = 15.6$ K [13], respectively.

While the majority of studies on the optical and magnetic properties α-$RuCl_3$ has focused on the bulk material, only little is known about the materials' properties after exfoliation. This is an important aspect, as the delamination of the crystal goes in hand with a reduction of the stacking disorder, which is discussed to be responsible for an enhanced onset of the antiferromagnetic ordering [1, 10]. Although it was recently demonstrated that α-$RuCl_3$ can be exfoliated by chemical [10], and electrochemical exfoliation [14], in both examples the material loses its pristine electronic and magnetic properties due to electron doping. To avoid this, an alternative liquid exfoliation strategy is sonication assisted liquid phase exfoliation (LPE), which relies on mechanical delamination by forces exerted on the starting material, created upon collapse of cavitation bubbles [15–18] and colloidal stabilisation through suitable surfactants or solvents [19–21]. This methodology has been applied to over 15 classes of layered materials, which have been successfully exfoliated into 2D-nanostructures, including transition metal dichalcogenides (TMDs) [22–24], transition metal hexathiohypodiphosphates ($M_2P_2S_6$) [25, 26], III–VI and IV–VI semiconductors [27–29], pnictogens [30–32], silicates [33], oxides [34, 35], hydroxides [36], and other minerals [37], as well as synthetic structures, such as organic polymers [38], 2D covalent organic frameworks [39, 40] and others. Typically, no phase transition or strong doping is observed so that it might be a suitable approach to study layer number dependent properties of α-$RuCl_3$.

To this end, we apply the additive free delamination of α-$RuCl_3$ by sonication assisted LPE under inert conditions. To address the impact of the layer number on the optical and magnetic response, samples were size-selected following previously established centrifugation-based techniques [41]. The lateral size and thickness distribution of the α-$RuCl_3$ nanosheets in the fractions was quantified by statistical atomic force microscopy (AFM). The structural integrity of the nanosheets was confirmed by a combination of transmission electron microscopy (TEM), Raman spectroscopy, x-ray diffraction (XRD) and x-ray photoelectron spectroscopy (XPS) measurements. In addition, the magnetic susceptibility of α-$RuCl_3$ was studied for three samples of different nanosheet size distributions in dispersion and for drop-cast samples, respectively. Furthermore, extinction and absorbance measurements on nanosheet dispersions were used to reveal systematic changes of the photo spectroscopic response. This allows to extract metrics for the material concentration, and the average layer number. Finally, time and temperature dependent absorbance measurements were used to study and to quantify the environmental stability for different nanosheet sizes.

2. Results and discussion

2.1. Preparation and characteristics of the nanomaterial

α-$RuCl_3$ crystals were grown by chemical vapour transport as reported in literature (see SI, experimental section for details) [42]. The layered character can be observed by SEM, revealing crystallites up to a size of approximately 1 mm (see SI, figure S1). The crystallinity of the starting material is confirmed by Raman spectroscopy and powder XRD (see SI, figure S2).

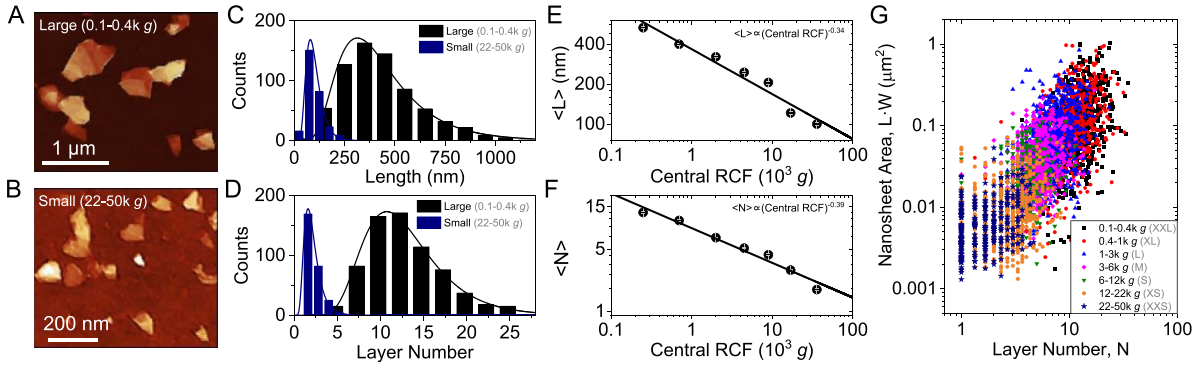

Figure 1. AFM statistics on fractions of size-selected α-$RuCl_3$: (A), (B) AFM images of drop cast nanosheets for two fractions containing relatively large, ((A), 0.1–0.4k *g*) and small ((B), 22–50k *g*) nanosheets. (C), (D) histograms of lateral sheet size (C) and layer number (D) distribution for the two fractions shown in (A) and (B). The histograms for the large fraction are depicted in black, the histograms for the small fraction in blue (for the other fractions see SI, figure S4). (E) Mean lateral size of nanosheets across all fractions on a double logarithmic scale. Note, that we define the length as the longest dimension of a sheet. (F) Mean layer number of nanosheets across all fractions on a double logarithmic scale. The AFM apparent height is converted into layer number by step height analysis on terraces on the sheets (see SI, figure S3 for details). The solid lines are linear fits, highlighting the power law dependence for both, $<L>$ and $<N>$ with the central centrifugation speed between two steps. (G) Scatter plot of the nanosheet area (product of length and width) as a function of their layer number across the different fractions of the size selection.

Ground single crystals were exfoliated under inert gas conditions in dried, distilled, and degassed *N*-cyclohexyl-2-pyrrolidone (CHP) assisted by bath sonication. CHP was chosen as exfoliation medium as pyrrolidone-based solvents are known to be suitable stabilising solvents for LPE of various layered crystals and additionally can promote surface passivation supressing material decomposition [25, 43]. The latter is associated to strong interactions of the solvent with the nanosheet surface and the formation of a protective solvation shell [43, 44]. After exfoliation, the as-obtained stock dispersion of the nanomaterial was size-selected by liquid cascade centrifugation (LCC) [41] to split the initially polydisperse nanosheet mixture of different sizes and thicknesses into fractions of well-defined size distributions. To this end, consecutive centrifugation steps were applied, starting with a step at low centrifugal acceleration (i.e. 100 *g*), which leads to sedimentation of large and thick nanosheets. The resulting supernatant was separated from the sediment and used for the subsequent step at higher centrifugation speed (i.e. 400 *g*). After this, and the following centrifugation steps, the sediment was redispersed in reduced volume of fresh solvent to yield a concentrated nanosheet dispersion for further analysis. Note that the unit *g* refers to a relative centrifugal force (RCF) expressed in multiples of the earth's gravitational acceleration. The same procedure was followed for centrifugation at 1k *g*, 3k *g*, 6k *g*, 12k *g*, 22k *g*, and 50k *g*, whereas the first sediment and the final supernatant were both discarded, as they contain mostly unexfoliated, and defective material, respectively. Following this method, seven fractions of α-$RuCl_3$ nanosheets with different size and thickness distributions were produced, suitable for further analysis. For consistency with previous reports, we label the fractions by the lower and upper boundary of the centrifugal acceleration used for trapping nanomaterial between two consecutive steps. For example, the sediment from centrifugation of the supernatant after 3k *g* at 6k *g* is labelled as 3–6k *g*.

To quantify the size and thickness distribution in the individual fractions of the size selection, statistical AFM measurements were performed on drop-cast nanosheets on Si/SiO_2 wafer fragments after dilution of the concentrated samples with isopropanol (see SI, experimental section for details). For measuring the dimensions of the nanosheets, line profiles are extracted. We define the nanosheet length as the longest dimension of a sheet, while the width is the dimension perpendicular to the length. The height of a sheet is extracted from the average height from both profiles. An example is given in the SI, figures S3(A) and (B) (for further details, see [23, 45]). Representative images of the fractions containing the largest (0.1–0.4k *g*) and the smallest (22–50k *g*) nanosheets isolated within the boundaries of the size selection are shown in figures 1(A) and (B). The corresponding distributions of the lateral sizes and the nanosheet layer number of the same two fractions are shown in direct comparison in figures 1(C) and (D), respectively. Note that for the accurate determination of the layer number from the measured apparent AFM thickness, additional contributions from impurities, solvent residues, chemical potential, and the measurement parameters must be considered. The measured apparent height in liquid-exfoliated nanosheets is thus typically overestimated, but proportional to the expected crystallographic thickness [25, 40, 46–51]. This issue can be overcome by a step height analysis on incompletely exfoliated nanosheets to convert apparent AFM thickness to layer number [25, 40, 46, 47, 52]. In brief, the AFM height of a single layer is determined by measuring line profiles on nanosheets with suitable steps and terrace structures (see SI, figure S3(C) for an example). Plotting the step height on >100 structures in ascending order reveals regular steps with a height of multiples of 1.5 nm in

the case of LPE α-$RuCl_3$ (see SI, figure S3(D)). Hence, the measured, apparent nanosheet height is divided by 1.5 nm for conversion into layer number.

Both fractions shown in figure 1 exhibit a lognormal lateral size (length L, figure 1(C)) and thickness (layer number N, figure 1(D)) distribution which is shifted towards significantly smaller sizes for the fraction isolated at higher centrifugation speed (22–50k g). A comparison of the size and thickness distributions of all fractions isolated by LCC is shown in the SI (figures S3 and S4). Upon further analysis, the arithmetic mean values of the nanosheet length, $<L>$ and layer number, $<N>$ are plotted as a function of the midpoint of the two consecutive centrifugation steps used to produce the fraction (central RCF) on a logarithmic scale (figures 1(E) and (F)). In both cases, a clear decrease of both dimensions is observed with increasing centrifugal acceleration, following a power law dependence. Fitting the data reveals proportionalities for $<N> \propto \overline{\mathrm{RCF}}^{-0.34}$ and $<L> \propto \overline{\mathrm{RCF}}^{-0.39}$. Note that a similar behaviour is observed for other 2D-material systems [53], even though an exponent of -0.5 is typically expected for $<L>$ due to the correlation between $<L>$ and the cut size, which is found to be proportional to the inverse rotation rate, as reported elsewhere [41, 54]. To further visualise the change of the dimensionality of the nanomaterial in each fraction of the size selection sequence, the area of individual nanosheets found in the different size fractions is shown as function of their layer number in a scatter plot where each data point represents an individual sheet (figure 1(G)). The graph clearly shows the decrease of the average nanosheet size with increasing centrifugation speed, as well as some overlap of the nanosheet dimensions represented in adjacent fractions. In addition, it shows that thinner nanosheets tend to be smaller and thicker nanosheets tend to be larger. This is typical for LPE nanosheets and due to both delamination and nanosheet tearing occurring [55].

To confirm the crystallinity and structural integrity of the nanosheets, a combination of TEM, Raman spectroscopy, XPS and XRD measurements was performed on the exfoliated nanomaterial. The results of the microscopic and spectroscopic characterisation are summarised in figure 2. For TEM, a non-size selected dispersion, where only unexfoliated material was removed as sediment at 100 g, was drop-cast on Quantifoil TEM grids in N_2 atmosphere. This sample was chosen to avoid exposure to ambience as much as possible, since centrifugation had to be performed (in sealed vials) outside the glovebox. We note that CHP residues were removed in the prevacuum of the microscope ($\sim 2 \times 10^{-5}$ mbar) at 150 °C for 40 min prior to low dose high resolution (HR)-TEM measurements (see SI, figures S5(A)–(D) for further details). A TEM overview image, including a relatively large nanosheet of several μm in length is shown in figure 2(A). The nanosheets shown on the image exhibit sharp edges, in good agreement with the morphology of the material characterised by AFM measurements. Selected area electron diffraction (SAED) was measured on the region indicated by the dashed circle and is shown in the inset of figure 2(A). The diffraction pattern shows sharp and bright spots confirming the crystallinity of the exfoliated nanomaterial. Figures 2(B) and (C) show HRTEM images of exfoliated α-$RuCl_3$ nanosheets, revealing the atomic lattice. The results from HRTEM are in good agreement with a simulated trigonal lattice structure (see SI, figures S5(E)–(H) for direct comparison of the measurement to expected patterns for different simulated $RuCl_3$ polymorphs) and previously reported literature [56]. The inset in figure 2(B) shows a fast Fourier transformed reciprocal space pattern of the probed region, further emphasising the crystalline character of the sample. In addition to SAED, scanning transmission electron microscopy (STEM) energy-dispersive x-ray (EDX) mapping was performed on free-standing nanosheets. The magnified high-angle annular dark field (HAADF) STEM image and the elemental distribution maps for ruthenium (red), chlorine (green) and oxygen (white) are shown in figure 2(D). The measurements confirm the material's stoichiometry, and suggest only minute oxidation. This finding is further supported by core-loss electron energy loss spectroscopy (see SI, figures S6(A)–(C)). The average EDX spectrum on the sample shown in figure 2(D) and EDX measurements on additional nanosheets are shown in the SI (figures 6(D)–(F)). Based on EDX measurements, the material stoichiometry is suggested to be $RuCl_{2.6}O_{0.02}$, $RuCl_{2.7}O_{0.3}$ and $RuCl_{3.1}O_{0.01}$ for the different probed areas, respectively. Note that small and thin nanosheets show high electron beam sensitivity at 80 kV indicated by substantial changes of the nanosheet lattice upon beam irradiation. Hence, no further quantitative analysis is possible on ultrathin samples. Examples on the impact of the electron beam on thin α-$RuCl_3$ nanosheets are shown and discussed in the supporting information (see figures S6(G) and (H)).

To additionally assess the nanomaterials' structural integrity after the exfoliation and size selection, in particular for small/thin nanosheets that cannot be reliably probed in TEM, measurements on ensembles of nanosheets were performed. To this end, samples of different nanosheet sizes were drop-cast in an inert atmosphere on a gold coated aluminium support for Raman spectroscopy and XPS measurements (figures 2(E) and (F)) and on a quartz substrate for powder XRD measurements (figure 2(G)). The Raman spectra of three different sizes representative for large, intermediate, and small nanosheets (i.e. 0.1–0.4k g, 6–12k g and 22–50k g) are shown in figure 2(E), together with an average spectrum measured on a single crystal. The spectra are shown with horizontal offset for clarity. While all modes from the bulk material can also be observed in the exfoliated nanosheets, a significant broadening of the modes is observed for the exfoliated material, which can be attributed to finite size-effects, and random orientation of the drop-cast material. We note that a similar effect has also been observed for micromechanically-cleaved nanosheets [4]. As no additional modes appear in the spectra of the nanosheets, no clear indications for material decomposition after LPE and LCC can be observed by Raman measurements. However, species formed upon decomposition may not be Raman active or resonant with the excitation wavelength.

Hence, XPS measurements were additionally performed. The ruthenium 3d core level spectrum is shown in figure 2(F)

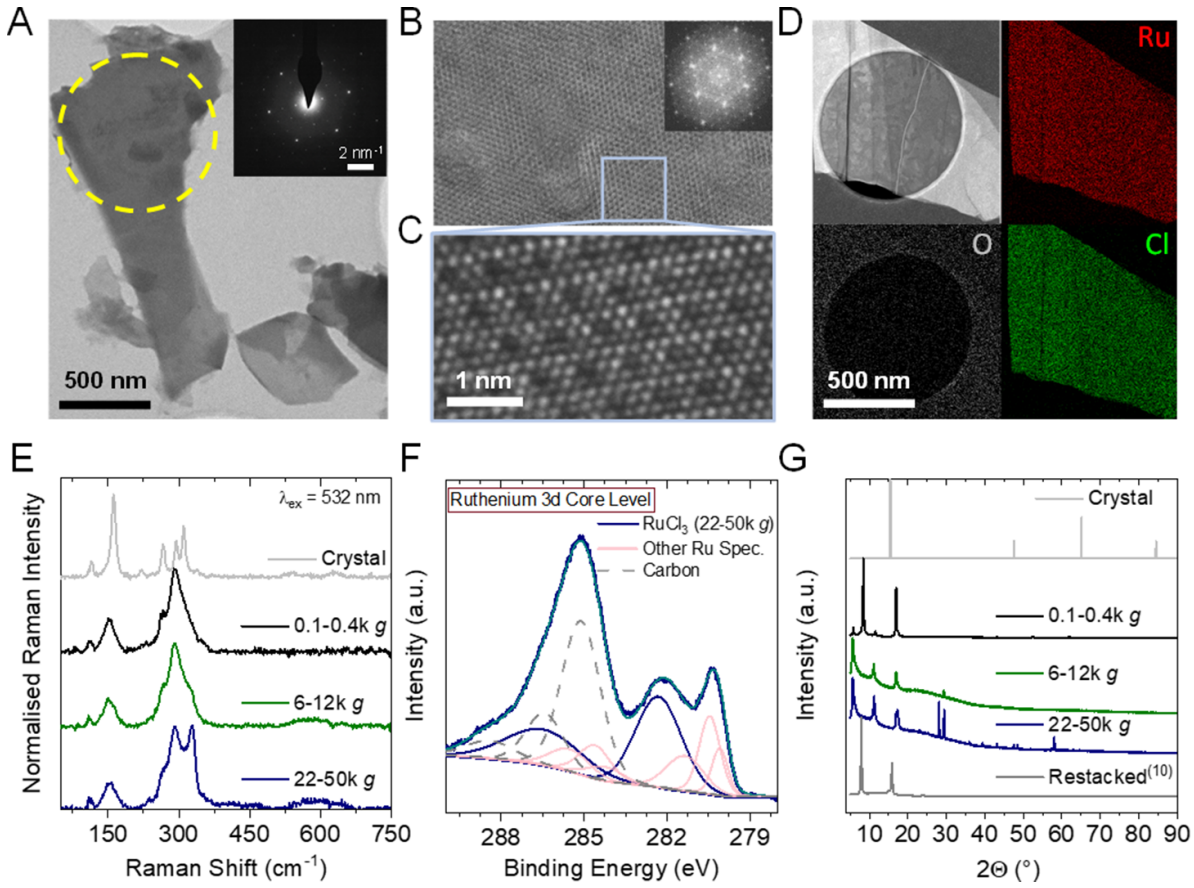

Figure 2. Structural integrity of α-$RuCl_3$ nanosheets: (A)–(D) TEM characterisation of individual nanosheets. (A) Low magnification bright field TEM image of multiple α-$RuCl_3$ nanosheets. The inset shows an SAED pattern corresponding to the spot indicated by the dashed circle, indicating high crystallinity of the sample. (B), (C) HRTEM image, revealing the crystal lattice of a α-$RuCl_3$ nanosheets in atomic resolution. The inset shows the local diffractiograms in reciprocal space. (D) HAADF image and EDX elemental distribution maps of ruthenium (red), chlorine (green), and oxygen (white). Overall, the TEM measurements indicate high crystallinity and structural integrity of the exfoliated nanosheet specimen. (E) Raman spectrum ($\lambda_{ex} = 532$ nm) of a bulk crystal (grey) compared to measurements on fractions representative for large (0.1–0.4k *g*, black), intermediate (6–12k *g*, green) and small (22–50k *g*, blue) nanosheet sizes, respectively. Similar modes are observed for the exfoliated nanomaterial as for bulk material. We note that a significant broadening of the modes is observed, which can be attributed to random orientation of the material upon drop casting. (F) Ruthenium 3d core level x-ray photoemission spectrum of a fraction containing the smallest nanosheets (22–50k *g*). Data fitting suggests that only ∼50% of the material surface is composed of α-$RuCl_3$ at the time of the measurement. (G) In-plane PXRD measurements ($\lambda = 1.54059$ Å) of a bulk crystal (grey) compared to different size-selected fractions of exfoliated nanosheets deposited on a quartz support in transmission geometry. Reported data on restacked $RuCl_3$ nanosheets is shown for comparison. The data for restacked nanosheets was modified and reproduced with permission from [10].

for the sample containing the smallest fraction of nanosheets (22–50k *g*). In addition to the expected signals from $RuCl_3$, additional contributions from carbon, elemental ruthenium, ruthenium oxide, -hydroxide and -oxyhydroxide (RuO_2, $Ru(OH)_3$, and $RuO(OH)_2$) are identified. The spectra suggest that only about 50% of the initial $RuCl_3$ is retained on the surface of the sample. Fitting of the data to the response from the individual components implies that ∼10% of the signal stems from elemental ruthenium, ∼21% from RuO_2 and 16% from $Ru(OH)_3$. A similar composition was found for a sample prepared the same way as the dispersion used for TEM (only removal of unexfoliated material), as shown in figure S7. This seems to disagree with TEM analysis on individual flakes. However, we note that XPS is surface sensitive and that the samples might have been exposed to ambient atmosphere (oxygen and water) prior to the measurement during sample transport even though they were sealed in a vacuum bag in the glovebox (see SI methods). Further, we note striking changes in the ruthenium 3d core level spectra on prolonged exposure. A set of four subsequent measurements on the same sample area is displayed in figure S7. Clearly, the $RuCl_3$ nanosheets are extremely sensitive also to the x-ray irradiation in spite of the ultrahigh vacuum conditions. Overall, the percentage of oxides and hydroxide species increases, while the feature assigned to $RuCl_3$ drops to ∼30% relative contribution to the ruthenium core level spectrum (figure S7(E)). Hence, the contribution of decomposition products from XPS measurements is likely overestimated. Unfortunately, it is not possible to infer whether beam damage has already occurred during the first acquisition so that the composition of the smallest/thinnest nanosheets cannot be assessed.

For further characterisation, powder XRD measurements were performed (figure 2(G)). The diffractograms of the samples containing large, intermediate, and small nanosheets

show patterns distinct from bulk α-$RuCl_3$ which is shown in grey for comparison. In order to understand these differences, reflexes are additionally compared to the recently reported pattern of randomly restacked $RuCl_3$ nanosheets (dark grey trace) [10]. The most intense Bragg reflexes of the exfoliated nanomaterial are found at similar angles as the restacked material. In addition, a signal broadening is observed which is assigned to structural distortion of restacked material after drop casting, similar to the effects observed in the Raman spectra. A closer analysis reveals that an increasing number of unassignable reflexes is observed with decreasing material size which could suggest that crystalline degradation products are formed, which are observed more clearly in the samples with higher surface to volume ratio. However, an alternative interpretation of the data could be that these are due to preferred orientation effects which are less prominent in the smaller sheets so that out-of-plane reflections become more dominant compared to larger sheets, where mostly reflections with (001) character can be observed due to the reflection geometry. This would imply that the other reflexes at higher angles (2Θ) are assignable to other $RuCl_3$ polymorphs or decomposition products. However, to confirm this, simulations for different crystal lattices and stacking orientation would be required, in particular because the reflexes cannot be assigned to the expected species from XPS measurements [10, 57, 58]. Overall, the bulk characterisation clearly shows that exfoliated α-$RuCl_3$ is prone to degradation which is discussed in more detail below. Since the material is exposed to ambient conditions during most measurements, unambiguous conclusions about the degree of oxidation cannot be obtained. However, results from TEM measurements, where the exposure to oxygen and water was minimised are encouraging and reveal only minute oxidation for the—as prepared—nanomaterial. Unfortunately, the smallest/thinnest nanosheets are very sensitive to beam damage both in TEM and XPS, so that their composition cannot be precisely assessed. However, as we will demonstrate below, absorbance spectra show the same spectral profile across all size-selected fractions which indicates a similar initial composition, also for the fraction of smallest/thinnest nanosheets. In the following, this will be analysed in more detail and also used to track degradation as function of time and temperature after exposure to ambient atmosphere which results in significant changes of the spectral profile. Overall, the results emphasize that extreme care must be taken upon preparation of liquid phase exfoliated nanomaterials due to significantly enhanced reactivity of the nanosheets compared to their bulk counterparts.

2.2. Magnetic characterisation of α-$RuCl_3$ nanosheets

As mentioned above, α-$RuCl_3$ is considered particularly interesting for fundamental studies of magnetic properties in low-dimensional structures and a possible realisation of a two-dimensional QSL in its ground state [10, 59–62]. To date, the majority of work was carried out on micromechanically-exfoliated (ME) nanosheets [4, 56, 63], with few examples of exfoliation in liquids [10, 14] and no report on pristine, undoped nanosheets as produced by sonication-assisted LPE. To this end, measurements in a superconducting quantum interference device on three different sizes, representative for large, intermediate, and small (i.e. 0.1–0.4k *g*, 6–12k *g* and 22–50k *g*) α-$RuCl_3$ nanosheets were performed in liquid environment and on drop-cast nanosheets, deposited in an inert atmosphere. The results of the magnetic measurements are shown figure 3. The low-temperature magnetic response of the different sizes of CHP-dispersed nanosheets are shown for two separate batches of exfoliated material. For clarity, a measurement on the starting material is included. Due to background uncertainties, resulting from non-negligible contributions from the solvent, the data was scaled to the susceptibility of the crystal at 50 K for better comparability. The bulk material shows a smooth Curie–Weiss like increase of the magnetisation upon cooling from room temperature, followed by a broad anomaly, indicative for the evolution of long-range antiferromagnetic order at around 10 K. This anomaly is suppressed in the large (0.1–0.4k *g*) nanosheet dispersion, and instead, a sharp transition is visible at $T = 2$ K (figure 3(A), inset). No such transition is observed for the smaller nanosheet sample (22–50k *g*) within the accessible temperature range. However, a similar transition can be observed for one out of the two batches of intermediate sized nanosheets (6–12k *g*) in $\partial(\chi T)\cdot\partial T^{-1}$ as illustrated in the inset of figure 3(A). We note that in general, the magnetic response at low temperatures differs between the respective batches for the small- and intermediate sized nanosheet dispersion, which we attribute to a combination of material decomposition, solvent effects and partial aggregation of dispersed nanosheets while approaching low temperatures.

To amend the magnetic response of the nanomaterial, free-standing nanosheet films of the individual sizes were prepared by drop casting of the dispersed material in a nitrogen atmosphere (see figure S8). The high-temperature magnetism for the different nanosheet size pellets is proportional to the bulk material, as evident by the susceptibility curves in figure 3(B). The platelets' susceptibilities deviate from that of the bulk material below ∼75 K, indicating stronger short range antiferromagnetic correlations in the bulk material than in the platelets. Both, the medium- and large-sized nanosheet films show a similar behaviour, exhibiting a broad plateau-like hump at around 4 K and a sharp decrease at the lowest accessible temperatures (figure 3(B), inset 1). The broad hump evolves into a well resolved peak if a low magnetic field is applied ($B = 0.01$ T, see figure 3(B), inset 2). This implies the evolution of long-range antiferromagnetic order at $T_N = 3$ K for the medium- and large-sized nanosheets, while the magnetic ordering is suppressed either completely or shifted towards temperatures below the accessible range when $B = 1$ T is applied. Further, size reduction stabilises the antiferromagnetic phase, as evidenced by a sharp peak in the susceptibility at $B = 1$ T at 2.2 K for the sample containing the smallest nanosheets (figure 3(B), inset 1). Note that due to the limited amount of material, measurements at $B = 0.01$ T were not successful for the smallest nanosheets. Despite the fact that long-range magnetic order in the small-sized platelets appears to

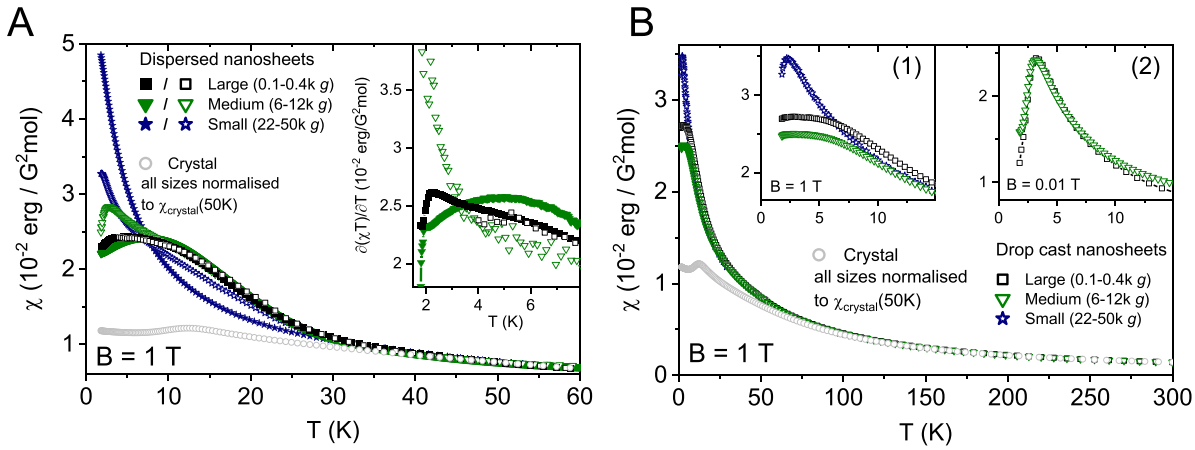

Figure 3. Magnetic characterisation of the exfoliated nanosheets: (A) Normalised magnetic susceptibility at $B = 1$ T as a function of temperature of the dispersed nanosheets for the same sizes as characterised in figure 2. A solid crystal was measured as reference (grey). Closed and open circles designate different sample batches. From each curve, a diamagnetic background signal was subtracted such that a subsequent normalising of the curve to the polycrystalline powder data at 50 K led to the maximal possible overlap at $40 < T < 60$ K. The inset shows the derivative $\partial(\chi T)\cdot\partial T^{-1}$ of the large- and medium-sized samples. (B) Normalised magnetic susceptibility of different sizes of deposited nanosheets at $B = 1$ T as a function of temperature. The data was corrected for a diamagnetic background and normalised to the crystals' susceptibility at 300 K. Inset (1) shows a magnified illustration of the main plot in the low temperature region. Inset (2) shows the magnetic susceptibility of the large- and medium-sized nanosheets obtained at $B = 0.01$ T for temperatures below 15 K.

be more pronounced compared to fractions containing larger nanosheets, the broad hump is not observed, which indicates less pronounced short-range antiferromagnetic correlations in this temperature regime. Hence, the overall tendency is that high-temperature antiferromagnetic correlations are suppressed upon size reduction while at the same time a sharp, rather 3D-like antiferromagnetic phase transition appears to be stabilised. One may argue that the low-temperature antiferromagnetic phase appearing in the solid nanosheet samples is of similar nature as the phase indicated by the sharp decrease in susceptibility of the solution-dispersed samples.

2.3. Optical properties of α-$RuCl_3$ nanosheets

To further shine light on size and thickness-dependent properties, the size-selected fractions of the α-$RuCl_3$ nanosheets were subjected to extinction and absorbance spectroscopy. For this purpose, photo spectroscopic measurements were performed in transmission mode, where $T = 10^{-\mathrm{Ext}}$ with $\mathrm{Ext} = \varepsilon \cdot c \cdot d$ (ε = extinction coefficient, c = concentration of the nanosheets and d = depth of the light path). We note that the measured extinction (Ext) is the combination of the wavelength dependent absorption (Abs) and scattering (Scat) contributions of the material, where $\mathrm{Ext}(\lambda) = \mathrm{Abs}(\lambda) + \mathrm{Scat}(\lambda)$. The dispersions were therefore additionally measured in the centre of an integrating sphere for the absorption measurements, where scattered light is collected (see experimental section). For a quantitative analysis, the concentration of each size-fraction was determined by gravimetric weighing of the exfoliated material.

That the scattering contribution is typically more pronounced for larger than for smaller particles of similar geometry is best illustrated by a direct comparison: figures 4(A) and (B) shows the wavelength dependence of the extinction (ε), absorption (α), and scattering (σ) coefficient of dispersions containing large (0.1–0.4k g) and a small (22–50k g) nanosheet sizes, respectively. A significant difference between the extinction and the absorbance coefficient is observed for the large nanosheets (figure 4(A)), which is almost negligible for the fraction containing the small nanosheets (figure 4(B)). Note that, compared to other LPE nanosheets such as TMDs, $Ni_2P_2S_6$, or layered hydroxides [22–25, 36], the contribution from scattering to the extinction spectra is much less pronounced [64].

The absorption and extinction coefficient spectra of all nanosheet sizes are shown in direct comparison in figures 4(C) and (D). All nanosheet sizes show two broad features at ∼370 and ∼550 nm. The inset in figure 4(D) depicts the change of the extinction coefficient as function of nanosheet size for three distinct wavelengths (400, 500 and 600 nm), which shows no significant variation with nanosheet size. This is an unusual observation as typically various effects lead to significant characteristic changes to the spectra of nanosheets of different sizes, including contributions from size-dependent light scattering as well as edge and confinement effects and from dielectric screening [25, 28, 46, 65, 66]. Those different effects influence the spectra in a characteristic way depending on the impact of the nanosheet size on the nanosheet geometry, and the band structure of the material. While size-independent optical coefficients are not usually observed, they enable the reliable determination of the α-$RuCl_3$ nanosheet concentration using the Beer Lambert law.

Due to the uncertainty in the masses extracted from gravimetry which have an impact on the coefficient spectra, size-dependent trends were additionally studied on normalised spectra. As shown in figures S9 and S10, the absorbance spectra only show very minor variations across the size-selected

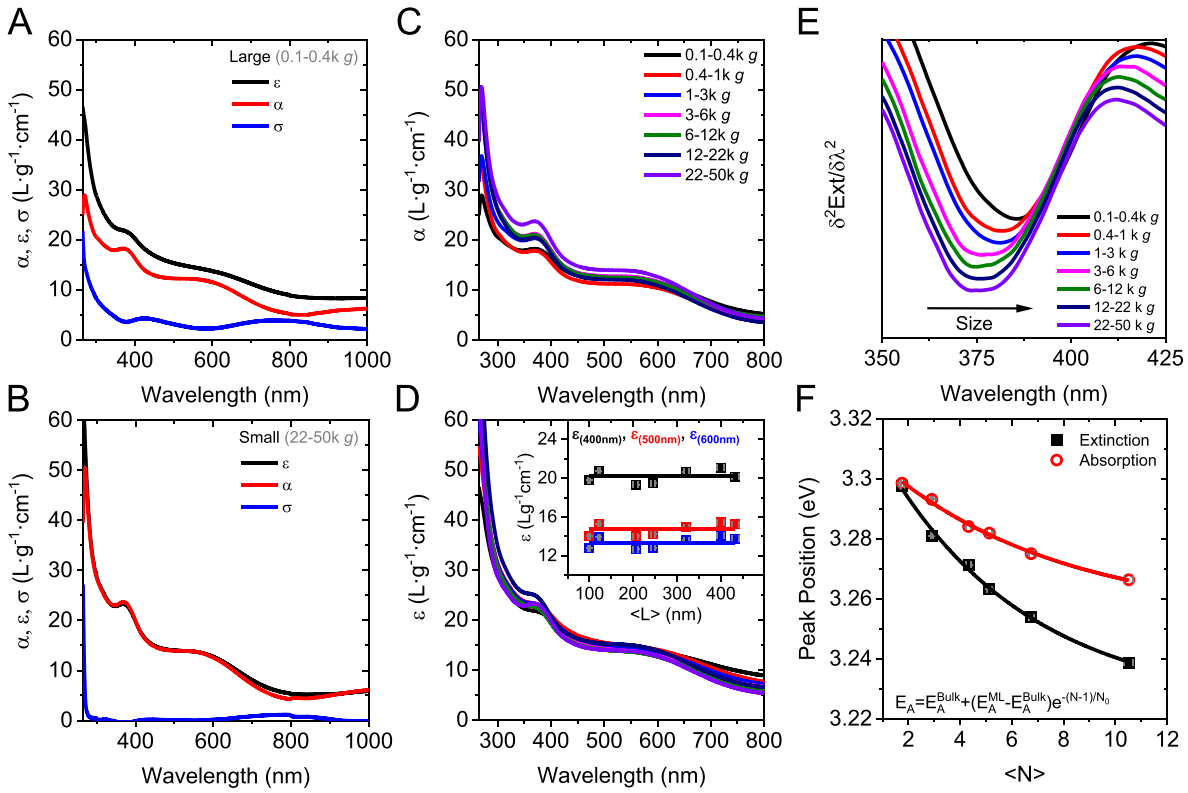

Figure 4. Metrics derived from optical spectroscopy. (A), (B) Extinction (ε), absorption (α) and scattering (σ) coefficient spectra for two nanosheet fractions containing relatively large nanosheets, ((A), 0.1–0.4k g) and small sheets, ((B), 22–50k g). The masses of the exfoliated material were determined by gravimetric filtering of the nanomaterial. (C), (D) Absorption (C) and extinction (D) coefficient spectra of all fractions in direct comparison. Minor changes with size of the material are observed. The extinction and absorption coefficients remain mostly constant across all fractions as indicated by the inset in (D) which shows the extinction coefficient at different wavelengths as a function of $<L>$. For further details see SI, figure S9. (E) Second derivative of the extinction used for the determination of the centre of mass peak positions. The transition shown red-shifts with increasing nanosheet dimensions. (F) Plot of the transition resonance as function of the mean layer number extracted from statistic AFM measurements.

fractions. However, we note that exposure to ambience, in particular at elevated temperatures, induces significant changes (figure S9) in the spectral profile. This indicates that the sample initially have the same composition and that degradation can be monitored through absorbance measurements. While changes across fractions in the normalised extinction and absorbance spectra are subtle, they are nonetheless systematic with size (see SI, figure S10(B) inset). Changes of the intensity ratios in extinction or absorbance spectra typically scale with the nanosheet lateral sizes due to different electronic contributions from the nanosheet edges and planes. Hence, the peak intensity ratio ($^{370\ \mathrm{nm}}/_{555\ \mathrm{nm}}$) is plotted as function of the average lateral nanosheet size in each fraction as determined from the statistical AFM analysis (see SI, figure S10(C)). This enables to fit the change of the spectra to a previously reported model (see table 1) [66]. While the fits are reasonable, we note that the magnitude of the change of the intensity ratios is too small for a reliable size determination from UV–Vis spectroscopy alone.

In addition to the size-dependent variation of the intensity ratio, systematic shifts of the optical transitions are observed in the spectra. These are often attributed to confinement and dielectric screening effects of excitons and typically scale with the nanosheet layer number [25, 46]. For a precise determination of the centre of mass peak position, the second derivative of the spectra is used, as shown in figure 4(E). A systematic redshift is observed for the peak at 375 nm in both, the extinction, and absorption spectra, as indicated by the arrow (for absorbance see SI, figure S10(D)). The resonance of the peak shows a well-defined scaling with the average nanosheet layer number, following an empiric equation, in agreement with previous reports (figure 4(F)) [24]. This is useful as it allows to quantify and compare phenomenological changes of electronic transitions with the average material layer number for different material systems, and to derive metrics for the layer number from extinction and absorbance spectroscopy. The results are shown in the table below (table 1).

We note that the resonances extracted from the extinction spectra are increasingly red-shifted for thicker nanosheets opposed to transition energies extracted from absorption spectra. This is attributed to an increasing contribution of light scattering from larger nanosheets, which is red-shifted compared to the absorbance (see also figure 4(A)).

Table 1. Fitting parameters for systematic changes of the extinction and absorbance intensity ratio and peak position with the average lateral nanosheet dimensions, $<L>$, and arithmetic mean layer number, $<N>$, respectively. Note that the change of the intensity ratio with nanosheet length is subtle and does not allow for a reliable platelet length determination from UV–Vis spectroscopy alone.

	$\langle L\rangle = \frac{B_1 - B_2 \cdot R}{A_2 \cdot R - A_1}$					$\langle N\rangle = 1 - \ln\left(\frac{E_A - E_{A,\mathrm{Bulk}}}{E_{A,\mathrm{ML}} - E_{A,\mathrm{Bulk}}}\right) \cdot N_0$		
Metric	R	$A_1(\mathrm{nm}^{-1})$	B_1	$A_2(\mathrm{nm}^{-1})$	B_2	E_A^{ML} (eV)	E_A^{Bulk} (eV)	N_0
Extinction	$\frac{370\ \mathrm{nm}}{555\ \mathrm{nm}}$	−0.0019	1.68	−0.0010	1	3.307	3.224	5.58
Absorbance		−0.0018	1.75	−0.0009	1	3.304	3.253	6.92

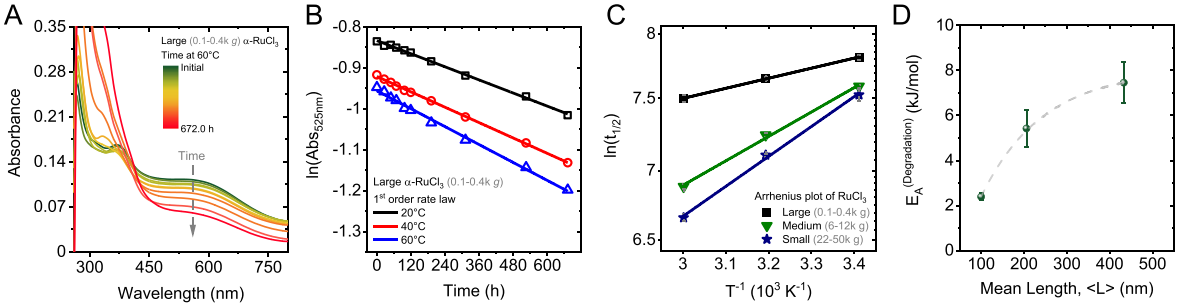

Figure 5. Change of the optical absorbance for different storage conditions as function of time. (A) Evolution of the extinction spectra for comparatively large α-$RuCl_3$ nanosheets (0.1–0.4k *g*) at 60 °C. (B) Plot of the natural logarithm of the optical density at 525 nm for absorbance measurements of comparatively large sized nanosheets stirred at 20 °C, 40 °C and 60 °C, respectively. A linearisation of the data is observed which implies that the decomposition follows a (pseudo) first order rate law. (C) Dependence of the macroscopic material half-life of α-$RuCl_3$ nanosheets as function of the inverse temperature on a semi-ln scale for different nanosheet sizes. The Arrhenius-type plot shows a linear dependence of the data points which enables to estimate the activation energy for the material decomposition. (D) Dependence of the activation energy on the average nanosheet length. The trend infers a preferential edge centred degradation mechanism.

2.4. Environmental stability of α-RuCl3 nanosheets

Nanosheets are often more sensitive to environmental decomposition or degradation compared to their corresponding bulk counterparts due to the largely increased surface area. It is therefore important to study the material stability for different nanosheet sizes and hence varying effective surface area. This is particular the case of α-$RuCl_3$, since some techniques suggested oxidation as discussed above. For a study on degradation kinetics, absorbance spectroscopy can be used to investigate the environmental impact on the nanosheets' optical properties as a function of size, time and temperature. To this end, dispersions containing nanosheets with different lateral sizes and thicknesses (being large—0.1–0.4k *g*, intermediate—6–12k *g*, and small—22–50k *g*) were exposed to ambient conditions and stirred at 20 °C, 40 °C and 60 °C, respectively, with absorbance spectra being acquired in defined time intervals. Prior to each measurement, samples were bath sonicated for ∼2 min to avoid potential impact from aggregation or material sedimentation. Absorption spectra of large-sized nanosheets, acquired at different stirring times, up to 672 h (28 days), at 60 °C are shown in figure 5(A). It is evident from significant changes of the spectral profile in the UV-region that the material undergoes substantial structural changes over time. In addition to obvious changes in the UV-region, the overall signal intensity of the material in the visible region (500 and 800 nm) decreases systematically over time where the initial shape of the spectral profile is retained. This suggests that within this wavelength range only contributions from $RuCl_3$ are detected, which can be used to quantitatively track the material decomposition as a function of time. We find that the change of the absorbance at 525 nm is best behaved for all nanosheet sizes and temperatures (for the full set of spectra, see SI, figure S11), following a single exponential decay (see SI, figures S12(A)–(C)).

Plotting the natural logarithm of the absorption at 525 nm as a function of the stirring time for different temperatures reveals a clear linearisation of the data, consistent with a (pseudo) first order rate law for the material degradation. Note that degradation kinetics in solution can be quite complex due to the formation of a solvation cage around the reagents, which may control the reaction rate due to diffusion effects. In addition, here, various reaction sites (e.g. edges and basal plane) are possible and different reaction products were observed in XPS (oxides and hydroxides). Therefore, a simple (pseudo) first order reaction would be more than surprising. However, in spite of an underlying complexity on the molecular level, the average macroscopic behaviour can apparently be approximated well with the (pseudo) first order kinetics. Therefore, we use a linear fit on the semi-ln scale to extract the macroscopic half-lives for the material decomposition. Note that the linear fit allows less degrees of freedom compared to an exponential fit and is thus more reliable for this purpose. The data is exemplarily shown in figure 5(B) for large (0.1–0.4k *g*) α-$RuCl_3$ nanosheets (for all sizes, see SI figures S12(D)–(F)). This is useful as it gives an idea about suitable conditions and the available timeframe for material processing (see table 2) and allows to estimate the activation energy of the material

Table 2. Half-lives of the nanosheet degradation extracted from fitting the (pseudo) first order decay kinetics obtained from following the absorbance as function of time for size-selected fractions of α-$RuCl_3$ containing large, medium and small nanosheets at three temperature. The activation energies of the degradation are also given.

Material fraction		$t_{1/2}\,(20^{\circ}\mathrm{C})$	$t_{1/2}\,(40^{\circ}\mathrm{C})$	$t_{1/2}\,(60^{\circ}\mathrm{C})$	$E_A\ \left(\mathrm{kJ\,mol^{-1}}\right)$
Large	(0.1–0.4k *g*)	2596 ± 46 h	2212 ± 25 h	1898 ± 49 h	18.9 ± 0.8
Medium	(6–12k *g*)	2083 ± 24 h	1440 ± 22 h	974 ± 20 h	15.4 ± 0.8
Small	(22–50k *g*)	1953 ± 84 h	1237 ± 14 h	769 ± 20 h	6.4 ± 0.2

decomposition from an Arrhenius type plot. The result of the latter is shown in figure 5(C), where the natural logarithm of the macroscopic material half-live is shown as a function of the corresponding inverse temperature. While only three temperatures were studied for each material size, a reasonable linearisation is found, which allows to approximate the size-dependent activation energy (see table 2). The trend is illustrated in figure 5(D), where the decomposition activation energy extracted from figure 5(C) is shown as a function of the average nanosheet size as determined from statistical AFM analysis. It is evident that the activation energy for the α-$RuCl_3$ degradation increases with the material size, which implies a lower activation energy for the material decomposition at nanosheet edges as opposed to the nanosheets' basal planes. While activation energies of the degradation are lower than for WS_2 monolayers in aqueous surfactant or $Ni_2P_2S_6$ [25, 67], we note that the half-lives are relatively long. This implies that, while the degradation of the material is observed at moderate temperatures already, the available timeframe until a significant portion of the material is affected from environmental impacts is reasonable for all material fractions studied within the scope of this work ($t_{1/2} > 30$ days), and is in agreement with previously reported results on aging effects on micromechanically-cleaved $RuCl_3$ nanosheets [4].

3. Conclusion

In conclusion, we demonstrated the additive free liquid exfoliation of α-$RuCl_3$ into nanosheets of different sizes and thicknesses in an inert atmosphere. The nanomaterial was separated into fractions of different size and thickness distributions, following established cascade centrifugation protocols. The structural integrity and crystallinity of individual nanosheets is confirmed by TEM measurements and further supported by a combination of Raman spectroscopy, XPS and XRD measurements, averaging over a large number of nanosheets. For the first time, susceptibility measurements were performed on α-$RuCl_3$ nanosheets in a liquid medium and compared to randomly restacked nanosheets in drop-cast samples. No QSL state could be confirmed for any of the exfoliated nanosheet sizes. In contrast, high-temperature antiferromagnetic correlations are suppressed upon size reduction while a sharp, 3D-like antiferromagnetic phase transition seems to be stabilised. Further, the photo spectroscopic response of α-$RuCl_3$ nanosheets for different size fractions allows to establish spectroscopic metrics for the average material layer number and concentration in dispersion. We emphasize that an unusually small change of extinction and absorbance intensity ratio with material lateral size is observed. While qualitatively similar to previously reported material systems [25, 66, 68], it is not considered as reliable metric due to the magnitude of the observed changes. At last, the material sensitivity to ambient oxygen and water was studied by time and temperature dependent absorbance measurements for different material sizes. The results suggest a macroscopic (pseudo) first order rate kinetic for the material decomposition which allows to estimate the available timeframe for further material processing and the activation energy for the degradation which is well below room temperature. An increasing trend of the activation energy with material size implies a preferentially edge-centred decomposition mechanism. We note that the observation of a relatively slow reaction with low activation energy (i.e. below room temperature) strongly suggests that kinetics on the molecular level are relatively complex so that the analysis should be considered as approximation.

We consider the presented results important for future applications exploiting magnetic properties of nanosheets. The low activation energy for the material decomposition emphasises that the exfoliation, storage and processing parameters can lead to significant differences in material characteristics attributed to partial oxidation of the nanomaterial and have to be studied carefully before applications can be considered.

Data availability statement

The data that support the findings of this study are available upon reasonable request from the authors.

Acknowledgments

This project has received funding from the European Union's Horizon 2020 research an innovation program under Grant Agreement No. 881603 (Graphene Flagship Core 3). K S acknowledge financial support by the Deutsche Forschungsgemeinschaft (DFG) through SY 217/1-1. GSD thanks the DTEC project Vital Sense for support. detec.bw is funded by the European Union – NextGenerationEU. C B acknowledges support from the German research foundation (DFG) under Grant Agreement Emmy-Noether, BA4856/2-1 and Jana Zaumseil for the access to the infrastructure at the Chair of Applied Physical Chemistry.

Conflict of interest

The authors declare no competing financial interests.

ORCID iDs

Kevin Synnatschke https://orcid.org/0000-0001-7018-9396
Martin Jonak https://orcid.org/0000-0002-4052-1340
Georg S Duesberg https://orcid.org/0000-0002-7412-700X
Bettina V Lotsch https://orcid.org/0000-0002-3094-303X
Claudia Backes https://orcid.org/0000-0002-4154-0439

References

[1] Cao H B, Banerjee A, Yan J Q, Bridges C A, Lumsden M D, Mandrus D G, Tennant D A, Chakoumakos B C and Nagler S E 2016 Low-temperature crystal and magnetic structure of α-$RuCl_3$ *Phys. Rev.* B **93** 134423
[2] Balents L 2010 Spin liquids in frustrated magnets *Nature* **464** 199–208
[3] Banerjee A *et al* 2016 Proximate Kitaev quantum spin liquid behaviour in a honeycomb magnet *Nat. Mater.* **15** 733–40
[4] Du L *et al* 2019 2D proximate quantum spin liquid state in atomic-thin α-$RuCl_3$ *2D Mater.* **6** 015014
[5] Knolle J, Kovrizhin D L, Chalker J T and Moessner R 2014 Dynamics of a two-dimensional quantum spin liquid: signatures of emergent Majorana fermions and fluxes *Phys. Rev. Lett.* **112** 207203
[6] Nayak C, Simon S H, Stern A, Freedman M and Das Sarma S 2008 Non-Abelian anyons and topological quantum computation *Rev. Mod. Phys.* **80** 1083–159
[7] Kubota Y, Tanaka H, Ono T, Narumi Y and Kindo K 2015 Successive magnetic phase transitions in α-$RuCl_3$: XY-like frustrated magnet on the honeycomb lattice *Phys. Rev.* B **91** 094422
[8] Sears J A, Songvilay M, Plumb K W, Clancy J P, Qiu Y, Zhao Y, Parshall D and Kim Y-J 2015 Magnetic order in α-$RuCl_3$: a honeycomb-lattice quantum magnet with strong spin-orbit coupling *Phys. Rev.* B **91** 144420
[9] Majumder M, Schmidt M, Rosner H, Tsirlin A A, Yasuoka H and Baenitz M 2015 Anisotropic Ru^{3+} $4d^5$ magnetism in the α-$RuCl_3$ honeycomb system: susceptibility, specific heat, and zero-field NMR *Phys. Rev.* B **91** 180401
[10] Weber D, Schoop L M, Duppel V, Lippmann J M, Nuss J and Lotsch B V 2016 Magnetic properties of restacked 2D spin 1/2 honeycomb $RuCl_3$ nanosheets *Nano Lett.* **16** 3578–84
[11] Wang L, Rocci-Lane M, Brazis P, Kannewurf C R, Kim Y-I, Lee W, Choy J-H and Kanatzidis M G 2000 α-$RuCl_3$/polymer nanocomposites: the first group of intercalative nanocomposites with transition metal halides *J. Am. Chem. Soc.* **122** 6629–40
[12] Fletcher J M, Gardner W E, Fox A C and Topping G 1967 x-ray, infrared, and magnetic studies of α- and β-ruthenium trichloride *J. Chem. Soc.* A 1038–45
[13] Kobayashi Y, Okada T, Asai K, Katada M, Sano H and Ambe F 1992 Moessbauer spectroscopy and magnetization studies of .alpha.- and .beta.-ruthenium trichloride *Inorg. Chem.* **31** 4570–4
[14] Lam D, Lebedev D, Kuo L, Sangwan V K, Szydłowska B M, Ferraresi F, Söll A, Sofer Z and Hersam M C 2022 Liquid-phase exfoliation of magnetically and optoelectronically active ruthenium trichloride nanosheets *ACS Nano* **16** 11315–24
[15] Pecha R and Gompf B 2000 Microimplosions: cavitation collapse and shock wave emission on a nanosecond time scale *Phys. Rev. Lett.* **84** 1328–30
[16] Hodnett M, Choi M J and Zeqiri B 2007 Towards a reference ultrasonic cavitation vessel. Part 1: preliminary investigation of the acoustic field distribution in a 25kHz cylindrical cell *Ultrason. Sonochem.* **14** 29–40
[17] Liang S, Shen Z, Yi M, Liu L, Zhang X, Cai C and Ma S 2015 Effects of processing parameters on massive production of graphene by jet cavitation *J. Nanosci. Nanotechnol.* **15** 2686–94
[18] Han J T *et al* 2014 Extremely efficient liquid exfoliation and dispersion of layered materials by unusual acoustic cavitation *Sci. Rep.* **4** 5133
[19] Hernandez Y, Lotya M, Rickard D, Bergin S D and Coleman J N 2010 Measurement of multicomponent solubility parameters for graphene facilitates solvent discovery *Langmuir* **26** 3208–13
[20] May P, Khan U, Hughes J M and Coleman J N 2012 Role of solubility parameters in understanding the steric stabilization of exfoliated two-dimensional nanosheets by adsorbed polymers *J. Phys. Chem.* C **116** 11393–400
[21] Coleman J N 2009 Liquid-phase exfoliation of nanotubes and graphene *Adv. Funct. Mater.* **19** 3680–95
[22] Ueberricke L, Coleman J N and Backes C 2017 Robustness of size selection and spectroscopic size, thickness and monolayer metrics of liquid-exfoliated WS_2 *Phys. Status Solidi* b **254** 1700443
[23] Backes C, Hanlon D, Szydlowska B M, Harvey A, Smith R J, Higgins T M and Coleman J N 2016 Preparation of liquid-exfoliated transition metal dichalcogenide nanosheets with controlled size and thickness *J. Vis. Exp.* **118** e54806
[24] Synnatschke K, Cieslik P A, Harvey A, Castellanos-Gomez A, Tian T, Shih C-J, Chernikov A, Santos E J G, Coleman J N and Backes C 2019 Length and thickness dependent optical response of liquid-exfoliated transition metal dichalcogenides *Chem. Mater.* **31** 10049–62
[25] Synnatschke K, Shao S, van Dinter J, Hofstetter Y J, Kelly D J, Grieger S, Haigh S J, Vaynzof Y, Bensch W and Backes C 2019 Liquid exfoliation of $Ni_2P_2S_6$: structural characterisation, size-dependent properties and degradation *Chem. Mater.* **31** 9127–39
[26] Synnatschke K *et al* 2023 Exfoliablity, magnetism, energy storage and stability of metal thiophosphate nanosheets made in liquid medium *2D Mater.* **10** 024003
[27] Harvey A *et al* 2015 Preparation of gallium sulfide nanosheets by liquid exfoliation and their application as hydrogen evolution catalysts *Chem. Mater.* **27** 3483–93
[28] John B B, Andrew H, Ruiyuan T, Victor V-M, Aideen G, Cian G, Madeleine B, Joshua P, Yanguang L and Jonathan N C 2020 Liquid phase exfoliation of GeS nanosheets in ambient conditions for lithium ion battery applications *2D Mater.* **7** 035015
[29] Brent J R, Lewis D J, Lorenz T, Lewis E A, Savjani N, Haigh S J, Seifert G, Derby B and O'Brien P 2015 Tin(II) sulfide (SnS) nanosheets by liquid-phase exfoliation of herzenbergite: IV–VI main group two-dimensional atomic crystals *J. Am. Chem. Soc.* **137** 12689–96
[30] Brent J R, Savjani N, Lewis E A, Haigh S J, Lewis D J and O'Brien P 2014 Production of few-layer phosphorene by liquid exfoliation of black phosphorus *Chem. Commun.* **50** 13338–41
[31] Lin S, Chui Y, Li Y and Lau S P 2017 Liquid-phase exfoliation of black phosphorus and its applications *FlatChem* **2** 15–37
[32] Gu J, Du Z, Zhang C, Ma J, Li B and Yang S 2017 Liquid-phase exfoliated metallic antimony nanosheets toward high volumetric sodium storage *Adv. Energy Mater.* **7** 1700447
[33] Stöter M, Rosenfeldt S and Breu J 2015 Tunable exfoliation of synthetic clays *Annu. Rev. Mater. Sci.* **45** 129–51

[34] Wang Y, Zhang Y-Z, Dubbink D and ten Elshof J E 2018 Inkjet printing of δ-MnO_2 nanosheets for flexible solid-state micro-supercapacitor *Nano Energy* **49** 481–8

[35] Hanlon D *et al* 2014 Production of molybdenum trioxide nanosheets by liquid exfoliation and their application in high-performance supercapacitors *Chem. Mater.* **26** 1751–63

[36] Harvey A *et al* 2016 Production of $Ni(OH)_2$ nanosheets by liquid phase exfoliation: from optical properties to electrochemical applications *Mater. Chem.* A **4** 11046–59

[37] Molina-Mendoza A J *et al* 2017 Franckeite: a naturally occurring van der Waals heterostructure *Nat. Commun.* **8** 14409

[38] Lange R Z *et al* 2020 Enriching and quantifying porous single layer 2D polymers by exfoliation of chemically modified van der Waals crystals *Angew. Chem. Int. Ed.* **59** 5683–95

[39] Leubner S, Bengtsson V E G, Synnatschke K, Gosch J, Koch A, Reinsch H, Xu H, Backes C, Zou X and Stock N 2020 Synthesis and exfoliation of a new layered mesoporous Zr-MOF comprising hexa- and dodecanuclear clusters as well as a small organic linker molecule *J. Am. Chem. Soc.* **142** 15995–6000

[40] Gosch J, Synnatschke K, Stock N and Backes C 2023 Comparative study of sonication-assisted liquid phase exfoliation of six layered coordination polymers *Chem. Commun.* **59** 55–58

[41] Backes C *et al* 2016 Production of highly monolayer enriched dispersions of liquid-exfoliated nanosheets by liquid cascade centrifugation *ACS Nano* **10** 1589–601

[42] Oppermann H, Schmidt M and Schmidt P 2005 Autotransport oder Selbsttransport—Systeme mit Gasphasentransporten unter dem eigenen Zersetzungsdruck *Z. Anorg. Allg. Chem.* **631** 197–238

[43] Hanlon D *et al* 2015 Liquid exfoliation of solvent-stabilized few-layer black phosphorus for applications beyond electronics *Nat. Commun.* **6** 8563

[44] Abellán G, Lloret V, Mundloch U, Marcia M, Neiss C, Görling A, Varela M, Hauke F and Hirsch A 2016 Noncovalent functionalization of black phosphorus *Angew. Chem., Int. Ed.* **55** 14557–62

[45] Backes C, Higgins T M, Kelly A, Boland C, Harvey A, Hanlon D and Coleman J N 2017 Guidelines for exfoliation, characterization and processing of layered materials produced by liquid exfoliation *Chem. Mater.* **29** 243–55

[46] Backes C *et al* 2014 Edge and confinement effects allow *in situ* measurement of size and thickness of liquid-exfoliated nanosheets *Nat. Commun.* **5** 4576

[47] Gibaja C *et al* 2016 Few-layer antimonene by liquid-phase exfoliation *Angew. Chem., Int. Ed.* **55** 14345–9

[48] Ridings C, Warr G G and Andersson G G 2012 Composition of the outermost layer and concentration depth profiles of ammonium nitrate ionic liquid surfaces *Phys. Chem. Chem. Phys.* **14** 16088–95

[49] Nemes-Incze P, Osváth Z, Kamarás K and Biró L P 2008 Anomalies in thickness measurements of graphene and few layer graphite crystals by tapping mode atomic force microscopy *Carbon* **46** 1435–42

[50] Nagashio K, Yamashita T, Nishimura T, Kita K and Toriumi A 2011 Electrical transport properties of graphene on SiO_2 with specific surface structures *J. Appl. Phys.* **110** 024513

[51] Szendrei K, Ganter P, Sànchez-Sobrado O, Eger R, Kuhn A and Lotsch B V 2015 Touchless optical finger motion tracking based on 2D nanosheets with giant moisture responsiveness *Adv. Mater.* **27** 6341–8

[52] Gibaja C *et al* 2019 Liquid phase exfoliation of antimonene: systematic optimization, characterization and electrocatalytic properties *Mater. Chem.* A **7** 22475–86

[53] Synnatschke K 2021 Liquid phase exfoliation and size dependent properties of van der Waals crystals, *Dissertation* (Heidelberg: Heidelberg University) p 1 Online-Ressource (249 Seiten)

[54] Walter J, Nacken T J, Damm C, Thajudeen T, Eigler S and Peukert W 2015 Determination of the lateral dimension of graphene oxide nanosheets using analytical ultracentrifugation *Small* **11** 814–25

[55] Backes C *et al* 2019 Equipartition of energy defines the size–thickness relationship in liquid-exfoliated nanosheets *ACS Nano* **13** 7050–61

[56] Ziatdinov M *et al* 2016 Atomic-scale observation of structural and electronic orders in the layered compound α-$RuCl_3$ *Nat. Commun.* **7** 13774

[57] Takeda T, Nagata M, Kobayashi H, Kanno R, Kawamoto Y, Takano M, Kamiyama T, Izumi F and Sleight A W 1998 High-pressure synthesis, crystal structure, and metal–semiconductor transitions in the $Tl_2Ru_2O_7-\delta$Pyrochlore *J. Solid State Chem.* **140** 182–93

[58] Kraus W and Nolze G 1996 Powder cell—a program for the representation and manipulation of crystal structures and calculation of the resulting x-ray powder patterns *J. Appl. Crystallogr.* **29** 301–3

[59] Modic K A *et al* 2020 Scale-invariant magnetic anisotropy in $RuCl_3$ at high magnetic fields *Nat. Phys.* **17** 240–4

[60] Wulferding D, Choi Y, Do S-H, Lee C H, Lemmens P, Faugeras C, Gallais Y and Choi K-Y 2020 Magnon bound states versus anyonic Majorana excitations in the Kitaev honeycomb magnet α-$RuCl_3$ *Nat. Commun.* **11** 1603

[61] Plumb K W, Clancy J P, Sandilands L J, Shankar V V, Hu Y F, Burch K S, Kee H-Y and Kim Y-J 2014 α-$RuCl_3$: a spin-orbit assisted Mott insulator on a honeycomb lattice *Phys. Rev.* B **90** 041112

[62] Kim H-S, Catuneanu A and Kee H-Y 2015 Kitaev magnetism in honeycomb α-$RuCl_3$ with intermediate spin-orbit coupling *Phys. Rev.* B **91** 241110

[63] Zhou B, Wang Y, Osterhoudt G B, Lampen-Kelley P, Mandrus D, He R, Burch K S and Henriksen E A 2019 Possible structural transformation and enhanced magnetic fluctuations in exfoliated α-$RuCl_3$ *J. Phys. Chem. Solids* **128** 291–5

[64] Harvey A, Backes C, Boland J B, He X, Griffin A, Szydlowska B, Gabbett C, Donegan J F and Coleman J N 2018 Non-resonant light scattering in dispersions of 2D nanosheets *Nat. Commun.* **9** 4553

[65] Griffin A *et al* 2018 Spectroscopic size and thickness metrics for liquid-exfoliated h-BN *Chem. Mater.* **30** 1998–2005

[66] Backes C, Paton K R, Hanlon D, Yuan S, Katsnelson M I, Houston J, Smith R J, McCloskey D, Donegan J F and Coleman J N 2016 Spectroscopic metrics allow *in situ* measurement of mean size and thickness of liquid-exfoliated few-layer graphene nanosheets *Nanoscale* **8** 4311–23

[67] Karger L, Synnatschke K, Settele S, Hofstetter Y J, Nowack T, Zaumseil J, Vaynzof Y and Backes C 2021 The role of additives in suppressing the degradation of liquid-exfoliated WS_2 monolayers *Adv. Mater.* **33** 2102883

[68] Szydłowska B M, Hartwig O, Tywoniuk B, Hartman T, Stimpel-Lindner T, Sofer Z, McEvoy N, Duesberg G S and Backes C 2020 Spectroscopic thickness and quality metrics for $PtSe_2$ layers produced by top-down and bottom-up techniques *2D Mater.* **7** 045027